SolarPACES 2024, 30th International Conference on Concentrating Solar Power, Thermal, and Chemical Energy Systems

Receivers and Heat Transfer Media and Transport: Point Focus Systems

https://doi.org/10.52825/solarpaces.v3i.2355

Published: 24 Nov. 2025

On the Accuracy and Computational Load of Fast 1D Models for Solar Receiver Parametric Studies

SolarPACES 2024

Carmine Sabia[1,*], Simone A. Zavattoni[1], and Maurizio C. Barbato[1]

[1]University of Applied Sciences and Arts of Southern Switzerland, Switzerland

*Correspondence: Carmine Sabia, carmine.sabia@supsi.ch

Abstract. A big challenge consists in maximizing the thermal efficiency of volumetric solar receivers that are used to collect solar energy and heat-up a heat transfer fluid in renewable energy systems. Parametric studies provide an undisputed aid in early design stages and fast computational models are important to rapidly test novel configurations. In this paper, a comprehensive analysis to assess the accuracy and the computational load of 1D and 3D models compared to relevant literature data is presented. A 1D finite volume model and a 1D explicit model based upon the thermal resistance network are built by solving the solid and fluid energy balances and results are compared to accurate 3D CFD simulations of a solar receiver consisting of a silicon-carbide absorbing structure. The calculated air and solid temperatures are compared to literature findings on a receiver test geometry for different heat transfer fluid velocities. Results show that fast 1D models provide very accurate results with a maximum error of 2%-5% with respect to the reference in a computational time of few seconds, two order of magnitude lower than the one needed by accurate 3D CFD simulations.

Keywords: Solar Receivers, 1D Models, Fast Solution, Parametric Studies, Heat Transfer

1. Introduction

The nowadays energy crisis and the necessity of reducing the global energy dependence on fossil fuels is pushing scientific research toward the improvement and optimization of renewable energy sources [1]. In this context, concentrated solar technology has attracted huge interest as it can be directly used to convert solar radiation into thermal energy and fulfill local power demand [2] or provide the energy required to carry out high-level processes such as the production of synthetic and sustainable fuels [3]. Solar receivers, which convert concentrated solar power into thermal power, are specifically designed to absorb and transfer energy to a heat transfer fluid (HTF) at various operating temperatures and for a variety of systems [4]. They can be divided onto three categories, namely surface, porous and particle receivers [5]. Once operated at high-temperature levels, e.g., > 600-700 °C, the thermal energy lost due to radiation becomes the dominating factor affecting the receiver efficiency. Because of that, volumetric (porous) receivers offer a great advantage, with respect to surface receivers, thanks to their ability of volumetrically absorbing the incoming concentrated solar radiation. This, combined with the HTF suction from front surface directly exposed to concentrated solar radiation, allows to reduce the absorber temperature at the front, hence minimizing the heat loss due to thermal radiation. Absorbing media are usually constituted by silicon carbide (SiC) [6] or alumina-based (Al_2O_3) [7] random and ordinate structures that volumetrically collect the incoming energy and the radiation re-emitted by the hot structure itself. The design of volumetric solar receivers is

still today a florid research field, and a proper geometry and thermal optimization is considered of paramount importance for increasing the efficiency of modern concentrated solar plants. Experiments constitute a precise and reliable way to characterize their performance, but such apparatus are usually very complex and extremely expensive [2]. To overcome this, a variety of models of different complexity have been proposed, ranging from analytical ones [8] to full 3D, real-scale, CFD simulations [9,10]. Since the set-up of detailed numerical simulations is often time-consuming, more agile and simpler models are generally preferred for performing parametric studies at early stages of the design. The present paper focuses on the development of two fast 1D models for a reference test case based upon: (i) the formalism of finite volumes and (ii) the thermal resistance network. Furthermore, the results of these agile models are compared to those of a full 3D CFD model at first and then with those of a relevant reference case taken from literature [11].

2. Geometry and Validation Case

The geometry of the test case model studied in this work consists of the cylindrical receiver shown by Fig. 1 [11]. The receiver has a diameter and a length of 50 mm while inlet and outlet regions of 80 mm and 130 mm length, respectively, are added to allow for flow development.

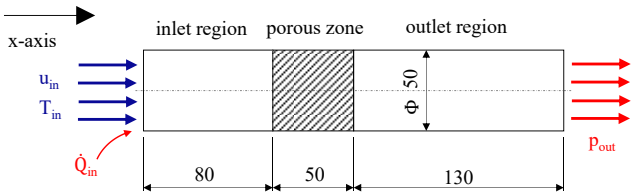

Figure 1. *Schematic of the test case receiver geometry, adapted from the work of Wu et al. [11].*

The boundary conditions are defined according to the reference case [11] for validation purposes. Two HTF velocities of 1.73 m/s and 2.16 m/s with a fixed inflow temperature of 27 °C are assumed while atmospheric pressure is set to the outlet. The concentrated solar radiation is 600 kW m^{-2} while a porosity of 80 % and an average pores diameter of 1.5 mm are considered for the isotropic and homogeneous ceramic foam constituting the porous zone. The pore-based Reynolds number gives a laminar flow condition with $Re_{d,max} < 200.1$.

3. Models description

3.1 1D FVM Model

The 1D finite volume (FVM) model is based upon the solution of energy balances for both the fluid and solid phases. The equations are solved through a 1D, cell-centered finite volume method employing the stencil depicted in Fig. 2.

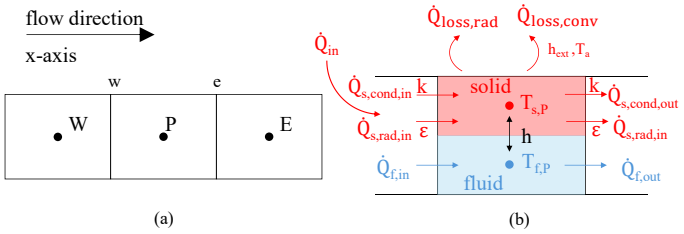

Figure 2. *Representation of the stencil used in the FVM discretization (l.h.s.) and scheme of fluid and solid energy fluxes for a generic "P" cell (r.h.s.). The schematic assumes that the HTF flows from left to right, with incident radiation entering from the left, and solid temperature reducing along the x-axis.*

Fig. 2 also shows all the relevant heat fluxes taking place for a generic cell "P" and, for each computational element, two equations accounting for the solid temperature, $T_{p,s}$, and fluid temperature, $T_{p,f}$, are solved. The energy balance for the solid phase can be written as:

$$\dot{Q}_{in} + \dot{Q}_{s,cond,in} + \dot{Q}_{s,rad,in} - \dot{Q}_{s,cond,out} - \dot{Q}_{s,rad,out} - \dot{Q}_{loss,conv} - \dot{Q}_{loss,rad} = h \cdot A_s \cdot \left(T_{s,P} - T_{f,P}\right) \quad (1)$$

while the energy balance for the fluid phase has the form:

$$\dot{Q}_{f,in} - \dot{Q}_{f,out} = h \cdot A_s \cdot \left(T_{s,P} - T_{f,P}\right) = \dot{m} \cdot c_p \cdot \left(T_{f,w} - T_{f,e}\right) \quad (2)$$

where $\dot{Q}_{in}$ is the incident solar radiation, $\dot{Q}_{s,cond,in}$ and $\dot{Q}_{s,cond,out}$ are the conductive powers, $\dot{Q}_{s,rad,in}$ and $\dot{Q}_{s,rad,out}$ are the radiative powers, while $\dot{Q}_{loss,conv}$ and $\dot{Q}_{loss,rad}$ are the thermal losses toward the ambient due to external convection and radiation, respectively. $\dot{m}$ [kg s^{-1}] is the mass-flow rate, c_p [J kg^{-1} K^{-1}] is the fluid specific heat at constant-pressure.

If the terms composing the left-hand side of Eq. 1 are made explicit, then the relation reads:

$$\dot{Q}_{in} + k \cdot A_k \left(\frac{T_{s,W} - T_{s,P}}{\Delta x}\right) + \varepsilon \cdot \sigma \cdot A_s \left(T_{s,W}^4 - T_{s,P}^4\right) - k \cdot A_k \left(\frac{T_{s,P} - T_{s,E}}{\Delta x}\right) - \varepsilon \cdot \sigma \cdot A_s \left(T_{s,P}^4 - T_{s,E}^4\right) - h_{ext} \cdot A_{ext} \left(T_{s,P} - T_a\right) - \varepsilon \cdot \sigma \cdot A_{ext} \left(T_{s,P}^4 - T_a^4\right) = h \cdot A_s \cdot \left(T_{s,P} - T_{f,P}\right) \quad (3)$$

where k [W m^{-1} K^{-1}] is the thermal conductivity, $A_k = A(1-\phi)$ [m^2] is simplified to the cross-section area participating to conductive heat transfer, Δx [m] is the grid size, ε [-] is the emissivity, σ [W m^{-2} K^{-4}] is the Stefan-Boltzmann constant, A_s [m^2] is the solid area participating to convective and radiative heat transfer, h_{ext} [W m^{-2} K^{-1}] is the convective heat transfer coefficient between the receiver external walls and the ambient and A_{ext} [m^2] is the external surface. The fluid temperature on the r.h.s. of Eq. 2 is discretized with a first-order upwind scheme and the upwind cell center value is used to approximate the temperature of the fluid at the face:

$$h \cdot A_s \cdot \left(T_{s,P} - T_{f,P}\right) = \dot{m} \cdot c_p \cdot \left(T_{f,W} - T_{f,E}\right) \quad (4)$$

The coefficient h, which regulates the convective heat transfer between the fluid and the solid phases is calculated exploiting the relation for the Nusselt number presented in [12,13]:

$$h = \frac{Nu \cdot k_f}{d^2 \cdot a_s} \quad (5)$$

and:

$$Nu = (32.054\phi^{0.38} - 109.94\phi^{1.38} + 166.65\phi^{2.38} + 86.98\phi^{3.38}) Re_d^{0.438} \cdot \quad (6)$$

where k_f [W m^{-1} K^{-1}] is the fluid thermal conductivity, d [m] is the pores diameter, Re [-] is the Reynolds number and a_s is the specific surface [13]:

$$a_s = 20.346\,(1-\varepsilon)\,\varepsilon^2\,\frac{1}{d_p} \quad (7)$$

Ambient temperature is applied to the first cell while, due to the fine grid and the negligible temperature variation expected in the last portion of the receiver, the temperature of the east face of the last element is set equal to its center cell value:

$$T_{1,w} = T_a \quad and \quad T_{n,e} = T_n \quad (8)$$

where subscripts 1, n and a indicate the first and the last computational cell and the ambient conditions, respectively. The incident solar radiation entering the porous media is modelled as an exponential decay through the Beer-Lambert law [14]:

$$\dot{Q}_{in}(x) = \dot{q}_0 A e^{-\beta x} \tag{9}$$

with β [m^{-1}] representing the extinction coefficient of the medium that is function of the pores diameter, d, and porosity, ϕ, [11]:

$$\beta = \frac{3(1-\phi)}{d} \tag{10}$$

Eq. 9 describes the solar radiation at a given position as function of the radiation intensity at the receiver front face, $\dot{q}_0$ [W m^{-2}], and its frontal area, A [m^2]. Eq. 10 shows that the extinction coefficient decreases with both porosity and pores diameter, meaning that a coarse structures with large pores allow for a better penetration of the incident radiation.

The pressure drop is computed according to the Darcy-Forchheimer equation

$$\nabla p = \frac{\mu}{K}\left(1 + \frac{\rho_f f \sqrt{K}}{\mu}|\mu|\right)u \tag{11}$$

where K [m^2] and f [-] are the permeability and the friction factor, respectively:

$$K = \frac{d^2}{1039 - 1002\phi} \tag{12}$$

$$f = \sqrt{K}\frac{0.5138\phi^{-5.739}}{d} \tag{13}$$

The fluid density and velocity are computed through the ideal gas law of Eq. 14 and the continuity constraint given by Eq. 15:

$$\rho_f = \frac{p}{R_{air}T_f}; \tag{14}$$

$$u = \frac{\dot{m}}{A \cdot \rho}. \tag{15}$$

Temperature dependent physical properties of air are accounted for through polynomial functions, valid in the 100-1'600 K range, given by Eq. 16, 17 and 18 [15]:

$$c_p = 1060 + 0.449T_f + 1.14 \cdot 10^{-3}T_f^2 - 8 \cdot 10^{-7}T_f^3 + 1.93 \cdot 10^{-10}T_f^4; \tag{16}$$

$$\mu = 1.13 \cdot 10^{-6} + 7.06 \cdot 10^{-8}T_f - 4.87 \cdot 10^{-11}T_f^2 + 2.66 \cdot 10^{-14}T_f^3 + 6.12 \cdot 10^{-18}T_f^4; \tag{17}$$

$$k_f = -3.94 \cdot 10^{-4} + 1.02 \cdot 10^{-4}T_f - 4.86 \cdot 10^{-8}T_f^2 + 1.52 \cdot 10^{-11}T_f^3; \tag{18}$$

The thermal conductivity of the absorber is kept constant at 120 W m^{-1} K^{-1}. The radiative contribution to the exchanged thermal power is linearized by decomposing the generic radiative power term written for two adjacent cells i and $i-1$ as reported in Eq. 19:

$$\varepsilon \cdot \sigma \cdot A_s\left(T_{s,i}^4 - T_{s,i-1}^4\right) = \varepsilon \cdot \sigma \cdot A_s\left(T_{s,i}^3 + T_{s,i}^2 T_{s,i-1} + T_{s,i-1}^2 T_{s,i} + T_{s,i-1}^3\right)\left(T_{s,i} - T_{s,i-1}\right) \tag{19}$$

The latter can be arranged so that the exponential temperature terms are calculated explicitly with known values at the previous iteration $(n-1)$, giving the linearized form of Eq. 20:

$$\varepsilon\sigma A_s\left(T_{s,i}^3 + T_{s,i}^2 T_{s,i-1} + T_{s,i-1}^2 T_{s,i} + T_{s,i-1}^3\right)\left(T_{s,i} - T_{s,i-1}\right) \approx \varepsilon\sigma A_s\left(T_{s,i}^{3,n-1} + T_{s,i}^{2,n-1} T^{n-1}{}_{s,i-1} + T_{s,i-1}^{2,n-1} T_{s,i}^{n-1} + T_{s,i-1}^{3,n-1}\right)\left(T_{s,i}^n - T_{s,i-1}^n\right) \quad (20)$$

Doing so, Eq. 3 and Eq. 4 can be solved iteratively in a fully coupled manner, obtaining a matrix-inverted solution stabilized availing of under-relaxation factors. The physical convergence is assessed examining the energy and mass balances with a maximum error that is lower than 0.1% in both cases.

3.2 1D Thermal Resistance Model

The second 1D model developed is based on the thermal resistance network concept which leads to the description of the physical phenomena involved, in the real system, through the realization of an equivalent thermal circuit (Fig. 3).

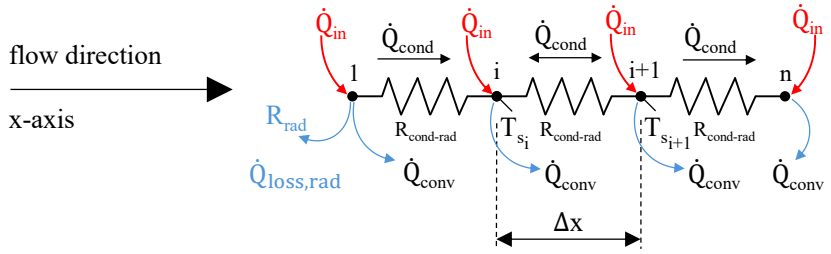

Figure 3. *Schematic of the fluxes entering and leaving the thermal resistances used to describe the case. The first (1), the last (n) and the generic cell (i) in the middle of the 1D model are depicted.*

The resulting balance equation, written in terms of thermal power and applied to each generic internal cell, reads:

$$\dot{Q}_{in,i} = \dot{Q}_{cond,i,i-1} + \dot{Q}_{cond,i,i+1} + \dot{Q}_{conv} \quad (21)$$

This equation can be further manipulated through the electric analogy:

$$\dot{Q}_{in,i} = \frac{T_{s,i} - T_{s,i-1}}{R_{cond-rad}} + \frac{T_{s,i} - T_{s,i+1}}{R_{cond-rad}} + a_S\, h\, (T_{s,i} - T_{f,i}) \quad (22)$$

Where the subscripts s and f indicate the solid and the fluid respectively, and a_S [1/m] is the specific surface area already defined in Eq. 7. h [W m^{-2} K^{-1}] is the convective heat transfer coefficient which, based upon the flow regime, can be calculated as [13]:

$$h = \frac{0.016\, \varepsilon\, k_f}{a_{sf}\, d_p^2}\, Pr^{0.33}\, Re_d^{1.35} \qquad Re_d \leq 75 \quad (23)$$

$$h = \frac{1.064\; k_f}{d_p}\, Pr^{0.33}\, Re_d^{0.59} \qquad Re_d \geq 350 \quad (24)$$

In case Re_d falls in between, a linear interpolation is applied to calculate the value of h [13]. While, concerning the equivalent thermal resistances, $R_{cond-rad}$ represents the conductive-radiative thermal resistance:

$$R_{cond-rad} = \frac{\Delta x}{\lambda_{eff}\, A\, (1 - \varepsilon)} \quad (25)$$

With Δx [m] indicating the grid spacing (see Fig. 3) and λ_{eff} [W m^{-1} K^{-1}] is the effective thermal conductivity of the porous medium accounting also for radiative heat transfer. Among various λ_{eff} correlations available [16-18], the authors selected the model provided by Gibson and

Ashby [19]. R_{rad}, acting on the first node of the equivalent thermal resistance network (see Fig. 3), accounts for the radiative losses of the receiver towards the environment [20]:

$$R_{rad} = \frac{1}{A\,\epsilon\,\sigma\left({T_{s,i}}^2 + T_{env}^2\right)\left(T_{s,i} + T_{env}\right)} \tag{26}$$

Where A [m^2] is the receiver frontal area, ϵ [-] the emissivity, σ [W m^{-2} K^{-4}] the Stefan–Boltzmann constant, T_s [K] and T_{env} [K] the solid and the environment temperature. Besides the absorber (solid) temperature, an additional energy balance equation was introduced with the aim of calculating the fluid temperature in each cell through the enthalpy variation:

$$\dot{Q}_{conv} = \dot{m}_f\,(h_{i+1} - h_i) \tag{27}$$

Where $\dot{m}_f$ [kg/S] and h [kJ/kg] are the fluid mass flow rate and the fluid enthalpy respectively. Once known the enthalpy, the fluid temperature was determined exploiting a polynomial function derived from tabulated (T, h) data for air assumed as ideal-gas [21], an iterative process was then applied to obtain the final values of the fluid and the solid temperatures. As final step, the pressure drop was calculated exploiting eq. 11.

3.3 3D CFD Model

The 3D CFD model of the receiver is simulated by resolving the Reynolds-Averaged Navier-Stokes (RANS) equations with Fluent code from Ansys. The symmetric nature of the receiver described in Ch. 2 is exploited and one fourth only of the geometry is modeled.

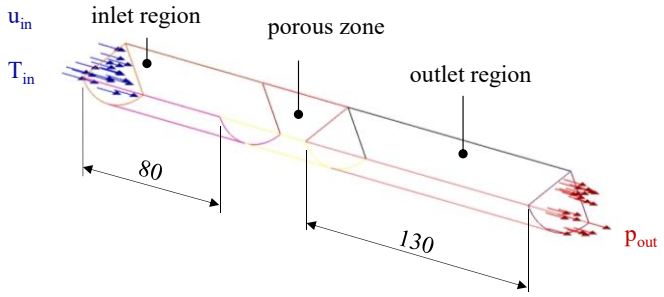

Figure 4. *Schematic of the 3D computational domain used for simulations. Velocity (u_{in}) and Temperature (T_{in}) are set at the inlet while pressure (p_{out}) is given as outlet boundary condition.*

A fully structured mesh composed by high quality hexahedral elements is built with Ansys Meshing. A maximum number of 234600 cells with a minimum orthogonal quality of 0.8 and a maximum aspect ratio of 4 is obtained. The 3D momentum and pressure-corrected mass balances are calculated for computing the air flow motion ensuring the satisfaction of the continuity constraint, while the energy equation is solved to model heat transfer. The fluid properties are defined according to the polynomials of Eq. 16, 17 and 18 and the boundary conditions are set as presented in Ch. 2. The presence of the absorber ceramic structure is considered through the porous medium approach with local thermal non-equilibrium (LTNE). The convective heat transfer coefficient and the incident solar radiation described by Eq. 6 and the Beer-Lambert law of Eq. 9 are implemented via user-defined functions (UDFs). Pressure velocity coupling is obtained through the SIMPLE algorithm of Patankar and Spalding [22] while gradients are discretized availing of second-order upwind schemes [22]. The numerical convergence is ensured by imposing residuals to 10^{-8} for energy and 10^{-5} for all the other equations.

5. Results and Discussion

Fig. 5 shows the temperature distribution of the HTF and the absorber along the receiver axis for a porosity of 0.8 and an average pores diameter of the structure of 1.5 mm. The temperature at which the fluid and solid stabilizes strongly depends on the air velocity since a larger heat transfer occur when this latter is augmented. The solid temperature variation with position is much smaller when the gas velocity is lower due to a less effective cooling given by the HTF. Results show that the proposed computational codes allow for a very accurate description of the temperature distribution along the reactor position, for both the fluid and solid phases, at any fluid velocity condition tested. It is interesting to notice that the highest difference is obtained between the reference and the CFD model due to simplified radiation modelling used in these latter simulations, that avails of an effective thermal conductivity of the porous medium which accounts for the effect of both conductive and radiative heat transfer.

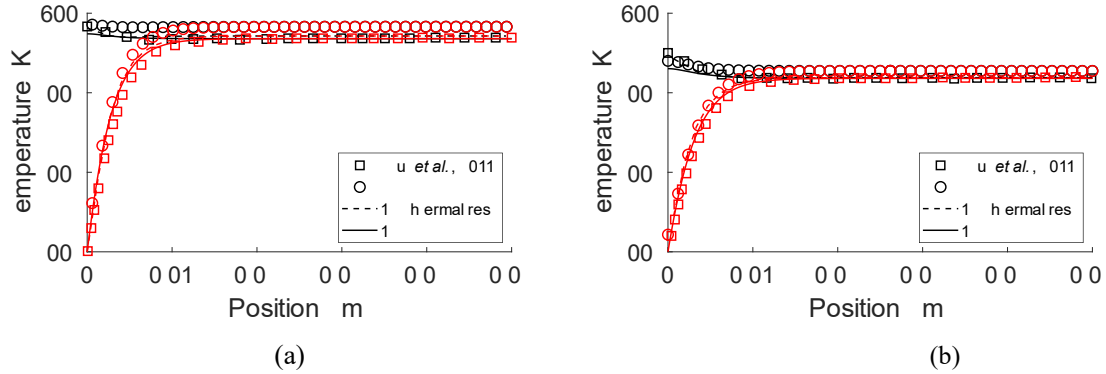

Figure 5. *Comparison between the temperature distribution along the receiver axis for a fluid inlet velocity of 1.73 m/s (a) and 2.16 m/s (b). Black and red lines/marker indicate solid and fluid temperatures, respectively. Results are obtained for a porosity ϕ = 0.8 and an average pores diameter d = 1.5 mm.*

Table 1 shows that a maximum error of about 2.3% is obtained between the fluid temperature data obtained from the 1D finite volume model and the reference for a simulation lasting 7.4 s of computational time. The maximum difference, simply estimated as reported by Eq. 28 where "num" refers to the numerical value while "ref" stands for the reference obtained from [11], is computed at each grid position and slightly increases when considering the 1D electro-thermal model and the full CFD case. The 1D simplified models very rapidly compute the temperature distribution in a simulation time which is two orders of magnitude smaller than the CFD one. All in all, simplified and fast 1D models are showed to be very effective for performing accurate parametric studies, providing reliable results in very rapid set-up and computational times and constituting a valid alternative to full CFD models in early stages of design or optimization.

$$e_{\max} = 100\frac{num - ref}{ref} \tag{28}$$

Table 1. *Maximum error, and computation time, comparison associated to the models presented and the reference case [11]. "e" stands for numerical difference while "ct" is the computational time needed to run a serial simulation on a Intel® Core™i5-3470 CPU @ 3.20GHz.*

Property	3D CFD	1D Electro-thermal	1D Finite Volume
e_{max} [%]	7.1	4.8	2.3
ct [s]	≈556.8	≈6.3	≈7.4

Data availability statement

Data can be made available upon specific request.

Underlying and related material

Specific information on the models developed can be given upon specific request.

Author contributions

Conceptualization: CS, SAZ; Data curation: CS; Formal Analysis: CS; Investigation: CS, SAZ; Methodology: CS, SAZ; Project Administration: CS, SAZ; Software: CS, SAZ; Validation: CS; Writing – original draft: CS; Writing – review & editing: SAZ, MCB.

Competing interests

The authors declare that they have no competing interests.

Acknowledgement

The authors gratefully acknowledge the work of the students Federico Erillo, Riccardo Facci, Ambrogio a ll'ara, Vincenzo Marrazzo and Anastasia Zatta.

References

[1] A.L. Ávila-Marín, "Volumetric receivers in Solar Thermal Power Plants with Central Receiver System technology: A review", Sol. Energy, 85, 891-910, 2011. https://doi.org/10.1016/j.solener.2011.02.002

[2] N.A. Cisneros-Cárdenas et al., "Thermal experimental study of a volumetric receiver-reactor using a Mini-Solar furnace", Appl. Therm. Eng., 234, 121276, 2023. https://doi.org/10.1016/j.applthermaleng.2023.121276

[3] S.A. Zavattoni, et al. "Numerical Performance Evaluation of the Synhelion Absorbing Gas Solar Receiver Under Different Operating onditions", AIP Conf. Proc., 110017, 2022. https://doi.org/10.1063/5.0085733

[4] R. Capuano et al., "Numerical models of advanced ceramic absorbers for volumetric solar receivers", Renew. Sustain. Energy Rev., 58, 656-665, 2016. https://doi.org/10.1016/j.rser.2015.12.068

[5] S. Mey-Cloutier et al., "Experimental study of ceramic foams used as high temperature volumetric solar absorber", Sol. Energy, 136, 2016. https://doi.org/10.1016/j.solener.2016.06.066

[6] G. Barreto et al., "Parametric analysis and optimization of porous volumetric solar receivers made of open-cell Si ceramic foam", Energy, 117476, 2020. https://doi.org/10.1016/j.energy.2020.117476

[7] J.M. Chavez, C. Chaza, " esting of a porous ceramic absorber for a volumetric air receiver", Sol. Energy Mat., 24, 172-181, 1991. https://doi.org/10.1016/0165-1633(91)90057-R

[8] A. Veeraragavan et al., "Analytical model for the design of volumetric solar flow receivers", Int. J. Heat Mass Transf. 55.4 (2012): 556-564. https://doi.org/10.1016/j.ijheatmasstransfer.2011.11.001

[9] S.A. Zavattoni et al., “ he Synhelion Absorbing Gas Solar Receiver for 1’ 0 0 ° Process Heat: CFD Modeling " AIP Conf. Proc. 2303, 030037 (2020). https://doi.org/10.1063/5.0029314

[10] M.I. Roldàn, J. Fernández-Reche, “ analysis of supercritical CO_2 used as HTF in a solar tower receiver" AIP Conf. Proc. 1734, 030031 (2016). https://doi.org/10.1063/1.4949083

[11] Z. Wu, et al. “ oupled radiation and flow modeling in ceramic foam volumetric solar air receivers". Sol. Energy, 85, 2374–2385, 2011. https://doi.org/10.1016/j.solener.2011.06.030

[12] Z. Wu et al., “Experimental and numerical studies of the pressure drop in ceramic foams for volumetric solar receiver applications". Appl. Energy, 87(2), 504-513, 2010. https://doi.org/10.1016/j.apenergy.2009.08.009

[13] C. Xu et al., "Numerical investigation on porous media heat transfer in a solar tower receiver". Renewable Energy, 36, 2011. https://doi.org/10.1016/j.renene.2010.09.017

[14] M.F Modest, "Radiative heat transfer - Third edition", Academic press, 2013. https://doi.org/10.1016/C2010-0-65874-3

[15] W. Liu, et al., “Design and Performance Analysis of Volumetric Solar Receiver Based on Porous Foam Ceramics”, AIP onf Proc , 2333, 040022, 2018. https://doi.org/10.1063/1.5067058

[16] Baillis, R oquard, “Radiative and onductive hermal Properties of o ams” 2008. https://doi.org/10.1002/9783527621408.ch11

[17] R. Coquard et al., “ onductive and Radiative Heat rans fer in e ramic and etal o ams at Fire Temperatures". Fire Technology, 48, 699–732, 2012. https://doi.org/10.1007/s10694-010-0167-8

[18] M. Mendes et al., “ etailed and simplified models for evaluation of effective thermal conductivity of open-cell porous foams at high temperatures in presence of thermal radiation". I.J. of Heat and Mass Transfer, 68, 612–624, 2014. https://doi.org/10.1016/j.ijheatmasstransfer.2013.09.071

[19] L Gibson, “ ellular solids” Cambridge University Press, 1997. https://doi.org/10.1017/CBO9781139878326

[20] F. Incropera, D. Dewitt, T. Bergman, A Lavine, “ undamentals of heat and mass transfer” John Wiley and Sons, 2007.

[21] Y. Cengel, A. ichael, “ h ermodynamics – An engineering approach”. McGraw-Hill Education, 2015.

[22] HK Versteeg, W Malalasekera, “An introduction to fluid dynamics: The finite volume method”, Prentice Hall, 007